Efficient on-axis SLM engineering of optical vector modes

Pascuala García-Martínez[1], David Marco[2], José Luis Martínez-Fuentes[3],
María del Mar Sánchez-López[2,4] and Ignacio Moreno[3]

1. Departamento de Óptica, Universitat de València, 46100 Burjassot, Valencia Spain
2. Instituto de Bioingeniería, Universidad Miguel Hernández de Elche, 03202 Elche, Spain
3. Departamento de Ciencia de Materiales, Óptica y Tecnología Electrónica, Universidad Miguel Hernández de Elche, 03202 Elche, Spain
4. Departamento de Física Aplicada, Universidad Miguel Hernández de Elche, 03202 Elche, Spain

Abstract

This work presents a method for the efficient experimental generation of arbitrary polarized vector beam modes. The optical system employs two liquid-crystal on silicon (LCOS) spatial light modulators (SLM) in a common path architecture, avoiding the use of beam-splitters. Each SLM displays a different phase-only mask, each one encoding a different pattern onto two orthogonal linear polarization components of the input beam. These phase-only masks are designed using a recently proposed random technique to encode complex amplitude values. This encoding technique reconstructs the complex function on-axis, thus avoiding incorporating carrier phases. By addressing such properly designed phase-only holograms we demonstrate arbitrary scalar modes on each polarization component, whose superposition results in a vector beam mode. Different superpositions of Laguerre-Gaussian and Hermite-Gaussian modes are obtained and the generated vector beam modes are analyzed. Moreover, the addition of a phase-bias proves itself useful to perform a phase-shifting technique in order to evaluate the correct phase of the generated vector beam.

1. INTRODUCTION

Vector beams (VBs), as light beams with defined spatially-variant intensity, phase and polarization features, are important for many applications including tight focusing [1], optical tweezing [2], materials processing [3], or super-resolution microscopy [4]. Cylindrically polarized optical beams with the radial or azimuthal polarization as paradigmatic cases, have attracted the most attention from researchers because of their special properties [5].

VBs can also be defined as pure laser modes with an additional spatial polarization modulation [6]. There have been several methods to generate such beams, based on the fact that they can be generated as the superposition of scalar modes having orthogonal polarization [7]. Initial techniques included the manipulation of a laser resonator in order to directly emit a desired vector beam [8], or the use of interferometric arrangements [9]. More recently, they have been generated with spatially variant uniaxial flat elements, which can be fabricated with subwavelength gratings [10], or with liquid-crystal materials [11]. These elements, often referred to as q-plates, are in general designed to generate low-order VBs [12,13]. However, higher-order Laguerre-Gaussian q-plates have also been developed [14].

An alternative method to generate vector beams is based on spatial light modulators (SLM). While these methods require bulky optical systems, their programmability offer a great flexibility, and several different optical arrangements have been proposed. The commonly used parallel-aligned liquid-crystal SLM can modulate only one polarization component, parallel to the liquid-crystal director. Therefore, in order to control two polarization components, they usually require either dividing the device screen in two halves [15,16], using two SLMs [17], or

passing the beam twice through the SLM after a proper polarization transformation [18]. In other schemes, the parallel generation (or detection) of VBs is accomplished by adding linear phase carriers [19,20]. Achromatic VBs have been obtained by using reflective digital micro-mirror SLMs, which are free from chromatic aberration, but require additional elements for polarization control [21]. In all these cases, the SLM operates externally to the laser cavity. However, laser modes have also been generated by inserting a reflective phase-only SLM in the laser cavity [22], thus achieving the controllable generation of Hermite-Gauss (HG) and Laguerre-Gauss (LG) scalar beams. A similar scheme was extended to generate VBs [23].

In all cases, the use of SLMs introduces an important efficiency loss. This loss primarily arises from the pixelated structure of the devices, which generates additional diffraction orders. Furthermore, the optical arrangements usually employ beam-splitters that reduce the power budget. For this reason, recent works report on highly efficient optical arrangements to generate vector beams [24,25]. In addition, the generation of higher-order beams requires some kind of amplitude modulation encoding. There have been many different proposals to achieve such amplitude encoding [26,27], which have been successfully applied to the encoding of different scalar beams [28-30]. In many cases, the amplitude encoding technique involves the use of a linear phase carrier and a consequent Fourier-filtering, which is mostly carried out off-axis, thus additionally contributing to a relevant reduction of the light budget and additional difficulties of stability and optical implementation. This operation, though, is sometimes mandatory when using SLMs that generate a strong DC component (usually due to flickering effects in the device) which prevents operating the system on axis [31].

In this work we combine recent advances to achieve an efficient way of generating VBs using SLMs. First, we use an optical setup based on two LCoS (liquid-crystal on silicon) SLMs arranged in a Z configuration. This type of configuration, already used in [32], is very robust, stable, and efficient since it has a common path for both polarization components and no beam splitters are required. We previously used this architecture for implementing a polarization diffraction grating based polarimeter [33] and customized structured polarized dual polarization split lenses [34]. In the new system here presented, though, we use two Hamamatsu LCoS-SLMs, devices that are free of flicker thus allowing operating the system on-axis, as opposed to the previous systems that were operated off-axis due to the zero-order (DC) component caused by this flicker effect. In addition, we use a recently developed method to encode complex valued computer-generated holograms (CGH) onto phase-only displays [35]. This method is based on a random spatial multiplexing of two phase-only diffractive patterns (the phase information of the desired signal pattern and a diverging optical element that controls the amplitude) and creates the desired hologram reconstruction on axis. Therefore, it is very efficient in terms of light budget since it does not require adding a carrier phase function and does not reduce the available space bandwidth product. This encoding technique was successfully applied to demonstrate a simultaneous aberration and aperture control in a visual simulator system [36], and here we experimentally apply it to generate VBs. By addressing different combinations of scalar modes belonging to the Orbital Angular Momentum (OAM) Poincaré sphere [37,38] encoded onto orthogonal polarization states, we build different VBs [39]. Finally, we demonstrate that our two SLM-based optical system enables to easily apply a phase-shifting technique that proves itself very useful to obtain the exact phase distribution of the superpositions of different generated modes.

The paper is organized as follows: after this introduction, Section 2 describes the optical system for the independent control of polarization components. Then, in Section 3 we explain the design of phase-only holograms for displaying complex-valued functions. Experimental results are shown in Section 4. In Section 5 we use phase-shifting techniques to estimate the phase of the optical beams finally obtained. Conclusions are given in section 6.

2. OPTICAL SYSTEM FOR THE INDEPENDENT CONTROL OF POLARIZATION COMPONENTS

Figure 1 shows the scheme of the optical setup. We use an input He-Ne laser (λ=633 nm) that is spatially filtered and collimated. Two LCoS-SLMs are arranged in a Z configuration. The angle between the incident ray and the reflected ray on each modulator is about 11°. LCoS1 and LCoS2 devices are on conjugated planes by means of a 4*f*-system obtained by two lenses of the same focal length, thus obtaining a minus one magnification. Both devices are parallel-aligned LCoS displays from Hamamatsu (model X10468-01). We measured a reflectivity of more than $R = 78\%$ for both devices. And they have 800×600 pixels, with 20 μm pixel pitch, an effective area of 15.8×12 mm^2 and 98% fill factor, thus providing more than 96% efficiency to the main reflected beam (zero order). Therefore, the total device efficiency at the zero order is about $\eta \sim 75\%$. As mentioned earlier, an important characteristic of these devices is that they are free of flicker. Therefore, the reflected beam does not present zero order (DC) component and the displayed holograms can be designed to generate reconstruction on-axis, and therefore make full use of this 75% zero-order efficiency.
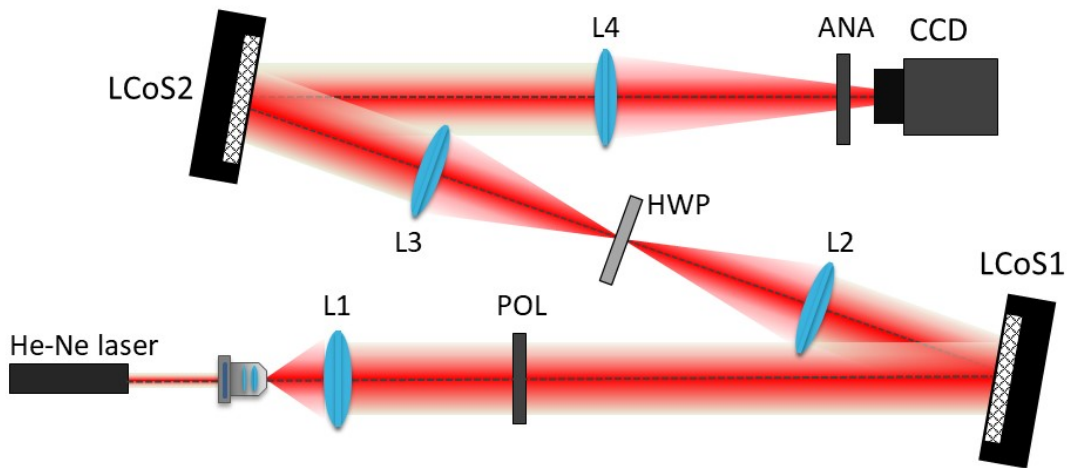

Fig. 1. Scheme of the optical setup. LCoS1 and LCoS2 are two liquid-crystal on silicon SLMs, with the liquid-crystal director oriented horizontally. A 4*f*-system (lenses L2 and L3) images LCoS1 onto LCoS2. POL: input linear polarizer. ANA: output polarization analyzer. HWP: half-wave plate. CCD: charge couple device detector.

The input polarizer (POL) is oriented at 45° to ensure equal magnitude on both horizontal and vertical polarization components. Parallel-aligned LCoS displays only modulate the linear polarization component parallel to the LC director. In our devices, this corresponds to the laboratory horizontal direction. Therefore, a phase pattern addressed to LCoS1 modulates the horizontal component of the input beam, while the vertical polarization component is unaffected. A half-wave plate (HWP) oriented at 45° is added after LCoS1 in order to transform the horizontal linear polarization component into the vertical component of the input beam (and viceversa). In this way, LCoS2-SLM modulates the polarization component that was not modulated by LCoS1-SLM, while leaving unaffected the polarization component that was already modulated by the first SLM. Thus, the output beam has two orthogonal horizontal and vertical polarization components that are independently modulated through the phase-only mask implemented by the two LCoS-SLMs.

The output beam emerging from the system is phase-only modulated in its vertical and horizontal components, and therefore the output Jones vector can be written as:

$$\vec{J}(x,y) = \begin{pmatrix} J_x(x,y) \\ J_y(x,y) \end{pmatrix} = \begin{pmatrix} e^{i\psi_1(x,y)} \\ e^{i\psi_2(x,y)} \end{pmatrix}, \tag{1}$$

where $J_x(x,y)$ and $J_y(x,y)$ denote the spatial pattern encoded onto the vertical and horizontal linear polarization components respectively, and $e^{i\psi_k(x,y)}$, $k = 1,2$, denotes the phase-only masks displayed onto LCoS1 and LCoS2 SLMs respectively. A lens focuses the beam, which is captured by a CCD camera. This final lens could be a physical converging lens or, as we use in this work, can be encoded onto the phase-only holograms $\psi_k(x,y)$ displayed on the LCoS SLMs. Finally, a polarizer analyzer (ANA) verifies the polarization output.

3. TECHNIQUE FOR ENCODING A COMPLEX FUNCTION ONTO A PHASE-ONLY SLM

Since LCoS devices work in phase-only modulation regime, a method to encode complex values onto phase-only displays is required. Here we used the codification method described in [35], which is based on a random spatial multiplexing of two phase-only functions: the phase information of the desired pattern and a diverging optical diffractive element to redirect undesired light out of the optical axis. This codification method presents interesting features: 1) it does not require any iterative algorithms, thus it is not computationally costly; 2) the desired complex optical field is reconstructed on-axis; and 3) no phase carriers are required. Next, we briefly review this method.

Let $F(x,y) = M(x,y)e^{i\varphi(x,y)}$ be the complex function to be encoded, where $M(x,y)$ and $\varphi(x,y)$ represent its magnitude and phase. A new multiplexed phase-only function $e^{i\psi(x,y)}$ is designed as:

$$e^{i\psi(x,y)} = R(x,y)e^{i\varphi(x,y)} + \bar{R}(x,y)e^{i\xi(x,y)}, \tag{2}$$

where $R(x,y)$ is a binary-amplitude (0-1) pattern, $\bar{R}(x,y) = 1 - R(x,y)$ is its complementary pattern, and $e^{i\xi(x,y)}$ is the phase function of a diverging element, in our case a high-frequency negative diffractive axicon, $\xi(x,y) = -2\pi r/p$, $r = \sqrt{x^2 + y^2}$ denoting the radial coordinate, and p denoting the axicon's period. The role of $R(x,y)$ is to select, at each pixel, between the phase function $\varphi(x,y)$ and the diverging axicon phase function $\xi(r)$.

The negative diffractive axicon acts as a circular blazed diffraction grating that diverges the light away from the optical axis. This light can be very easily filtered by a circular aperture. This way, the magnitude information $M(x,y)$ is encoded onto the new multiplexed phase-only function $\psi(x,y)$ via the function $R(x,y)$ which is defined as

$$R(x,y) = \begin{cases} 1 \text{ if } M(x,y) > rnd(x,y), \\ 0 \text{ if } M(x,y) \leq rnd(x,y), \end{cases} \tag{3}$$

where $rnd(x,y)$ is a distribution of random numbers in the interval [0,1].

This phase-only encoding technique of the complex function $M(x,y)e^{i\varphi(x,y)}$ can be easily understood as follows. If the required amplitude $M(x,y)$ is close to 1, it is better represented

4

by the phase-only function $e^{i\varphi(x,y)}$ and $R(x,y) = 1$ is the good choice. On the contrary, for pixels where $M(x,y)$ is close to 0, light should be removed. The diverging axicon performs this operation directing light out of the optical axis. Therefore, $R(x,y) = 0$ is the right choice for these pixels. For intermediate values of $M(x,y)$, Eqs. (2)-(3) provide an adequate random choice between the two phase-only functions.

Note that the light directed out of the optical axis by the encoded axicon involves the arising of a ring of light at the Fourier transform planes, while the hologram reconstruction appears on axis [35]. Therefore, this ring of light must be filtered in order to achieve good results. Since the diffractive axicon has a high spatial frequency, the filtering can be easily done by means of a circular aperture located in the Fourier transform planes. For the mask displayed in LCoS1-SLM, a circular aperture can be placed at the back focal plane of the lens after the SLM. In our case, the HWP circular mount acted as the circular aperture, thus blocking the ring generated by the first axicon. For the second mask displayed on the LCoS2-SLM, the ring of light appears in the plane where the CCD camera detector is placed, but outside the detector area which is centered on the final reconstruction. Therefore, it has no impact on the final image.

The accuracy of this encoding technique for the implementation of digital complex holograms was analyzed in detail in Ref. [35]. The signal-to-noise ratio and efficiency of the hologram reconstruction depends on the required amplitude modulation, as well as on the characteristics of the random function applied in the algorithm. The authors were able to achieve a hologram efficiency around 35%. In that work, the technique was applied to the generation of higher-order scalar Laguerre-Gauss (LG) and Hermite-Gauss (HG) laser modes. Here, we apply it for the generation of VBs in the optical system described in Section 2.

4. VECTOR BEAMS, ORBITAL ANGULAR MOMENTUM AND HIGHER-ORDER POINCARÉ SPHERES

Although VBs are natural solutions to the vectorial Helmholtz equation they are very often generated as coaxial superpositions of orthogonal scalar fields with orthogonal polarizations [7]. The system in Fig. 1 directly allows the superposition of different HG or LG modes encoded on the vertical and horizontal polarization states. The use of SLMs also enables us to add an extra constant relative phase (β) between the vertical and horizontal polarization components. This is equivalent to adding a linear retarder with retardance β and neutral axes oriented along vertical/horizontal directions. It is well-known that this is also very useful to provide different realizations of VBs. The output Jones vector in Eq. (1) can be approximated by

$$\vec{J}(x,y) = \begin{pmatrix} J_x(x,y) \\ J_y(x,y) \end{pmatrix} \simeq \begin{pmatrix} M_1(x,y)e^{i\varphi_1(x,y)} \\ M_2(x,y)e^{i\varphi_2(x,y)}e^{i\beta} \end{pmatrix}. \tag{4}$$

where the complex functions $M_k(x,y)e^{i\varphi_k(x,y)}$, $k = 1,2$, denote the magnitude and phase encoded on each polarization component. As mentioned earlier, in order to generate VBs we will encode the complex functions that correspond to HG or LG modes. We designed the functions $\varphi_k(x,y)$ to include the quadratic phase corresponding to a lens that replaces the final physical lens (L4) in the system in Fig. 1.

At this point, it is interesting to remind the relations between different generalized Poincaré spheres represented in Fig. 2. Figure 2(a) shows the standard Poincaré sphere, where each polarization state corresponds to a point on the sphere. The equator defines the linear states, while the circular right- and left-handed states:

$$\hat{\mathbf{e}}_{\mathbf{R}} = \frac{1}{\sqrt{2}}\begin{pmatrix} 1 \\ +i \end{pmatrix}, \hat{\mathbf{e}}_{\mathbf{L}} = \frac{1}{\sqrt{2}}\begin{pmatrix} 1 \\ -i \end{pmatrix}, \tag{5}$$

lie on the north and south pole respectively. In general, an elliptic state given by

$$\hat{\mathbf{e}}_{\alpha,\varepsilon} = \sin\left(\varepsilon + \frac{\pi}{4}\right)e^{-i\alpha}\hat{\mathbf{e}}_{\mathbf{R}} + \cos\left(\varepsilon + \frac{\pi}{4}\right)e^{i\alpha}\hat{\mathbf{e}}_{\mathbf{L}} \tag{6}$$

describes a polarization ellipse with azimuth α and ellipticity ε, which lies on the point with longitude and latitude angles $(2\alpha, 2\varepsilon)$ of the Poincaré sphere.

In this work we encode HG and LG modes on the $J_x(x,y)$ and $J_y(x,y)$ patterns. HG modes are exact solutions of the scalar paraxial wave equations in Cartesian coordinates. We consider an output beam at the waist plane $z = 0$, the complex amplitude can thus be written as:

$$HG_{mn}(x,y,\omega_0) = \frac{1}{\omega_0}\sqrt{\frac{2^{-(m+n-1)}}{\pi m!n!}} H_m\left(\frac{\sqrt{2}}{\omega_0}x\right) H_n\left(\frac{\sqrt{2}}{\omega_0}y\right) e^{-\left((x^2+y^2)/\omega_0^2\right)}, \tag{7}$$

where H_m is the m-th order Hermite polynomial, ω_0 is the beam waist, and x and y are the Cartesian coordinates. On the other hand, LG modes are expressed at the waist as

$$LG_p^\ell(r,\theta,\omega_0) = \frac{1}{\omega_0}\sqrt{\frac{p!2^{|\ell|+1}}{\pi(|\ell|+p)!}}\left(\frac{r}{\omega_0}\right)^{|\ell|} L_p^{|\ell|}\left(\frac{2}{\omega_0^2}r^2\right) e^{-(r/\omega_0)^2} e^{i\ell\theta} = A_{p\ell}(r)e^{i\ell\theta}, \tag{8}$$

where $L_p^{|\ell|}$ are the $p\ell$-th order Laguerre polynomials, and r and θ are polar coordinates. The term $A_{p\ell}(r)$ in this equation accounts for the radial part of the function and does not depend on the sign of ℓ, only on its magnitude. The mode order is $N = m + n$ for an HG mode and $N = 2p + |\ell|$ for a LG mode, respectively [37].

For simplicity, we will restrict to the first-order modes $(N = 1)$, for which the following relations exist [37]:

$$HG_{D/A} = \frac{1}{\sqrt{2}}(HG_{01} \pm HG_{10}), \tag{9a}$$

$$LG_0^{\pm 1} = \frac{1}{\sqrt{2}}(HG_{10} \pm iHG_{01}), \tag{9b}$$

where $HG_{D/A}$ denote the diagonal/antidiagonal HG modes. Alternatively, the HG beams can be composed of LG modes as

$$HG_{10} = \frac{1}{\sqrt{2}}(LG_0^1 + LG_0^{-1}), \tag{10a}$$

6

$$HG_{01} = \frac{-i}{\sqrt{2}}(LG_0^1 - LG_0^{-1}), \tag{10b}$$

$$HG_D = \frac{e^{-i\pi/4}}{\sqrt{2}}(LG_0^1 + iLG_0^{-1}), \tag{10c}$$

$$HG_A = \frac{e^{-i3\pi/4}}{\sqrt{2}}(LG_0^1 - iLG_0^{-1}). \tag{10d}$$

These relations, equivalent to those found when superposing polarization states, can be used to define the orbital angular momentum (OAM) Poincaré sphere [38]. This Poincaré sphere represents the superpositions of scalar first order HG and LG modes (Fig. 2b), where the equator contains the HG_{10} mode and their in-plane rotated versions, and the poles correspond to the LG_0^1 and LG_0^{-1} modes. Every point in the OAM Poincaré sphere, with longitude 2α and latitude 2ε, is obtained as the superposition of the LG_0^1 and LG_0^{-1} modes as

$$f(x,y) = \sin\left(\varepsilon + \frac{\pi}{4}\right)e^{-i\alpha}LG_0^1 + \cos\left(\varepsilon + \frac{\pi}{4}\right)e^{i\alpha}LG_0^{-1}. \tag{11}$$

Note that this expression is analogous o an elliptic state in Eq. (6).

Finally, Fig. 2(c) shows the higher-order Poincaré sphere of order one [39], which represents the first-order cylindrically polarized VBs. There is a one-to-one mapping between every point on the standard Poincaré sphere and the states in the first-order Poincaré sphere [40]. Each homogeneous polarization state generates one first-order vector beam when it traverses a q-plate device [12,41].

We note that different realizations of the higher-order Poincaré sphere can be obtained, depending on the orthogonal polarization states that are selected to encode the scalar modes. The Poincaré sphere in Fig. 2(c) [39] corresponds to the VBs generated when LG modes are encoded onto the circular polarization components, i.e., vector beams generated as:

$$\vec{V}(x,y) = \sin\left(\varepsilon + \frac{\pi}{4}\right)e^{-i\alpha}LG_0^{-1}\hat{\mathbf{e}}_{\mathbf{R}} + \cos\left(\varepsilon + \frac{\pi}{4}\right)e^{i\alpha}LG_0^1\hat{\mathbf{e}}_{\mathbf{L}}. \tag{12}$$

The transversal section of these vector beams consists in elliptical states with constant ellipticity, but azimuth that rotates following the polar coordinate. Similarly, the superposition of LG modes encoded onto the vertical and horizontal linear polarizations results in the generation of VBs where the transversal section shows polarization states with constant orientation, but where the ellipticity changes following the polar coordinate [42].

We make use of the above relations to generate different VBs by means of the experimental system described in Section 2 (Fig. 1).
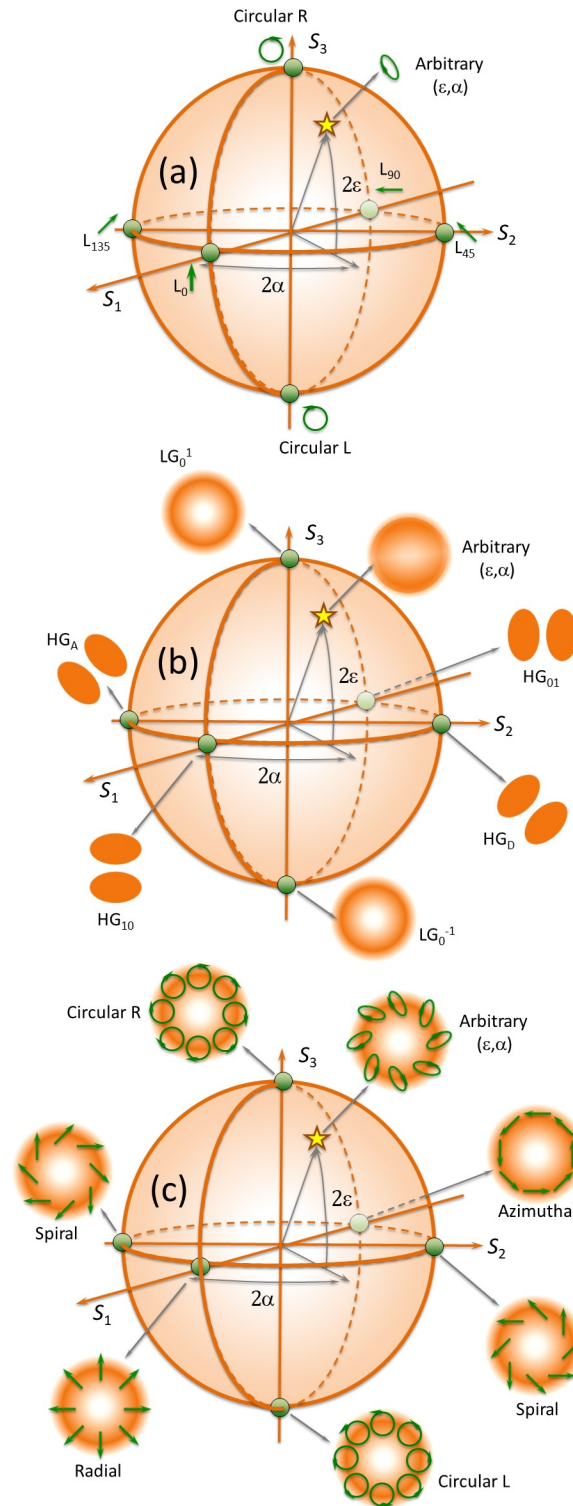
Fig. 2. (a) Standard Poincaré sphere for a homogeneous polarized state. (b) Orbital angular momentum (OAM) generalized Poincaré sphere. (c) Higher-order Poincaré sphere for first-order vector beams.

5. EXPERIMENTAL RESULTS

5.1 Superposition of orthogonally polarized HG modes

Let us start with the classical experiment that combines the HG_{10} and HG_{01} modes to generate a first-order vector beam [5]. The results are displayed in Fig. 3. In this case, we encode the mode HG_{10} on the vertical polarization, while the mode HG_{01} is encoded on the horizontal

polarization (note that the vertical direction is selected as the x axis). The output Jones vector is therefore given by

$$\vec{J}_1(x,y) = \frac{1}{\sqrt{2}}\begin{pmatrix} HG_{10}(x,y) \\ HG_{01}(x,y) \end{pmatrix}. \tag{13}$$

Figures 3(a) and 3(b) show a detail of the center of the phase-only hologram, codified using the technique presented in [35]. These masks show in the center the characteristic phase step of the HG beams (with a horizontal border for Fig 3(a), and a vertical border for Fig.3(b)) but accompanied by the high-frequency circular grating characteristic of the diffractive axicon.

Figure 3(c) shows the expected intensity and polarization pattern obtained from the Jones vector in Eq. (13), which corresponds to the radial polarization [5]. The inset shows the experimental CCD capture without analyzer, that exhibits the characteristic doughnut shape. The local state of polarization becomes evident when a linear analyzer is placed in front of the CCD camera. In Figs. 3(d) and 3(e) the analyzer is oriented vertical and horizontal, and only one polarization component is selected. The scalar modes HG_{10} and HG_{01} are then clearly visible. When the analyzer is oriented at ±45° the superposition of the two modes is built. The following simple Jones matrix calculus shows that the resulting field is

$$\vec{J}_{1P} = \frac{1}{2}\begin{pmatrix} 1 & \pm 1 \\ \pm 1 & 1 \end{pmatrix}\vec{J}_1(x,y) = \frac{1}{2}(HG_{10} \pm HG_{01})\frac{1}{\sqrt{2}}\begin{pmatrix} 1 \\ \pm 1 \end{pmatrix} \propto HG_{D/A}\hat{\mathbf{e}}_{\pm 45,0}, \tag{14}$$

where Eq. (9a) was applied and $\hat{\mathbf{e}}_{\pm 45,0}$ indicates the linear polarization states at ±45°. These superpositions, shown in Figs. 3(f) and 3(g), result in the diagonal and antidiagonal HG modes with polarized linear states oriented at ±45° respectively. Note how the projection of the polarization states in Fig. 3(c) agree with the intensity patterns in all cases. Note also that the rotation of the analyzer projects the generated vector beam onto a scalar mode that lies on the equator of the OAM Poincaré sphere.
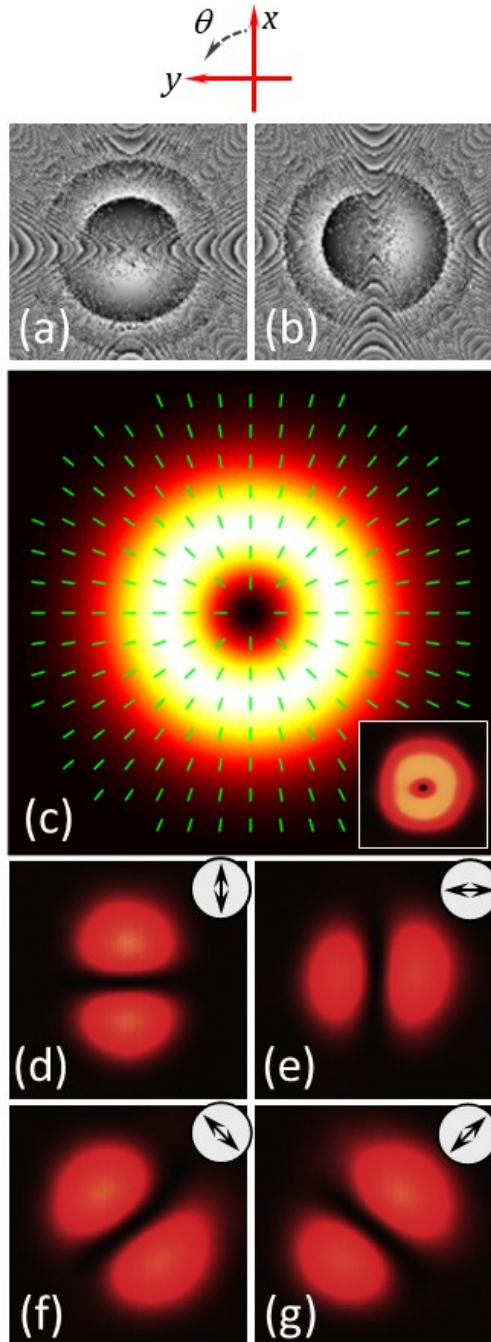
Fig. 3. (a)-(b) Central part of the phase-only holograms displayed on LCoS1 and LCoS2 to generate HG_{10} and HG_{01} modes. (c) Expected polarization pattern (the inset shows the CCD capture without analyzer). Experimental result with a linear analyzer oriented (d) vertical (HG_{10}), (e) horizontal (HG_{01}), (f) at 45° (HG_D) and (g) at −45° (HG_A). The analyzer's orientation is indicated on the top of each picture.

5.2 Phase bias control – Generation of LG modes from superposition of HG modes

Equation (9b) indicates that the LG modes can be obtained from the superposition of HG_{10} and HG_{01} modes with a relative $\pm\pi/2$ phase shift. The phase β in Eq. (4) can be changed simply by adding a constant gray level in one of the two phase holograms displayed on the LCoS-SLMs, in this case LCoS2. Therefore, we build a VB whose output Jones vector is in the form:

$$\vec{J}_2(x,y) = \frac{1}{\sqrt{2}} \begin{pmatrix} HG_{10}(x,y) \\ iHG_{01}(x,y) \end{pmatrix}. \tag{15}$$

Again, Figs. 4(a) and 4(b) show the holograms displayed on LCoS1 and LCoS2 SLMs. The polarization pattern in Fig. 4(c) looks different, since now it is the ellipticity (and not the orientation, as was the case in Fig. 3(c)) the polarization parameter that changes along the polar coordinate. Along the diagonal directions, the polarization becomes circular. This polarization map does not belong directly to the Poincaré sphere in Fig. 2(c), but it is simply the transmission of the radial polarization through a quarter-wave plate (QWP) with axes oriented along the $x - y$ coordinates [43]. Projecting the Jones vector in Eq. (15) onto a linear polarizer oriented at ±45° yields

$$\vec{J}_{2P} = \frac{1}{2} \begin{pmatrix} 1 & \pm 1 \\ \pm 1 & 1 \end{pmatrix} \vec{J}_2(x,y) = \frac{1}{2}(HG_{10} \pm iHG_{01}) \frac{1}{\sqrt{2}} \begin{pmatrix} 1 \\ \pm 1 \end{pmatrix} \propto LG_0^{\pm 1} \hat{\mathbf{e}}_{\pm 45,0}, \tag{16}$$

where we used Eq. (9b). The LG beams are obtained at linear states with orientation at ±45°.

The corresponding experimental results are shown in Fig. 4. In the absence of analyzer (inset in Fig 4(c)), the intensity adopts the same pattern as in Fig 3(c). However, when we place the analyzer, the spatial polarization patterns are revealed. Again, when the analyzer is oriented either vertical or horizontal, the scalar HG modes appear. However, when the analyzer is oriented at ±45°, the projection given by Eq. (16) results in the scalar modes $LG_0^{\pm 1}$. The polarization pattern in Fig. 4(c) is interesting since it allows transforming a vector beam onto scalar modes HG_{10}, HG_{01} and $LG_0^{\pm 1}$ by simply rotating the analyzer. Polarization ellipses drawn in blue are right states, while those in red denote left states. Linear states are drawn in green.
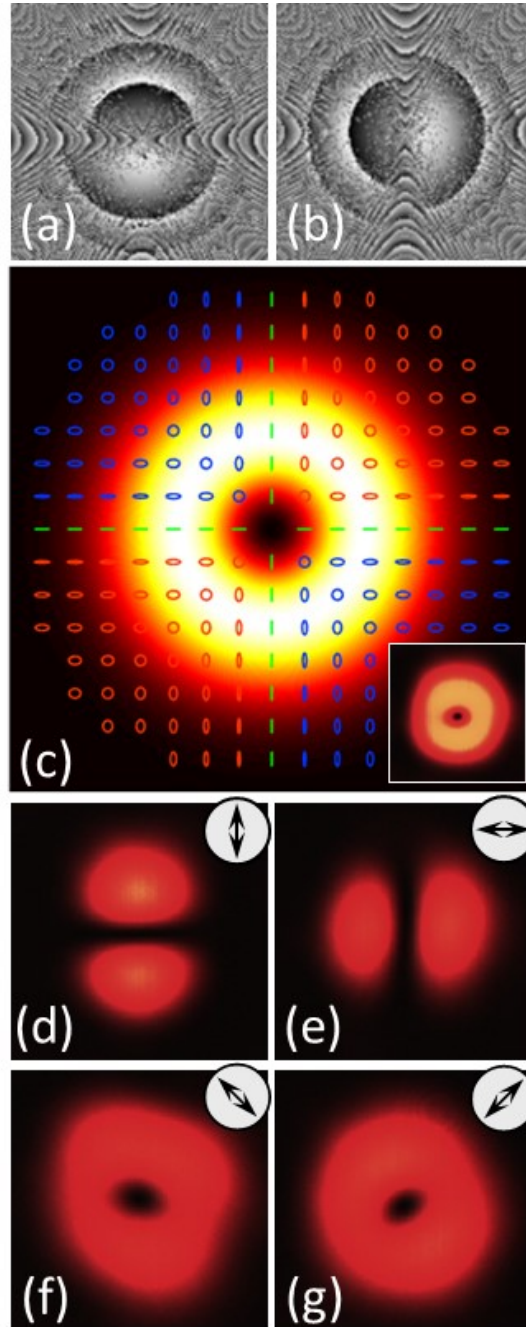
Fig. 4. (a)-(b) Central part of the phase-only holograms displayed on LCoS1 and LCoS2 to generate HG_{10} and HG_{01} modes. (c) Expected polarization pattern (the inset shows the CCD capture without analyzer). Ellipses with left- and right-handed polarization are drawn in red and blue respectively. Experimental result with a linear analyzer oriented (d) vertical (HG_{10}), (f) horizontal (HG_{01}), (g) at 45° (LG_0^1) and (h) at −45° (LG_0^{-1}). The analyzer's orientation is indicated on the top of each picture.

5.3 Stokes polarimetry of generated modes

The experimental images shown in Fig. 3 and Fig. 4 show the correct generation of the expected polarized beams. However, in the most general case the map of polarization states must be experimentally verified. This is typically done using an imaging polarimeter that provides images of the Stokes parameters. In order to complete the Stokes parameters measurement, two

additional images would be required in each case, using a quarter-wave plate (QWP) and a fixed polarizer to create a circular analyzer in front of the CCD camera.

However, alternatively, the QWP can be encoded with the aid of the SLMs, by adding a constant $\pm\pi/2$ phase shift to one of the two holograms. Note that, because we are considering paraxial beams, this is equivalent to the phase bias just mentioned in section 5.2. Adding a constant phase $\pm\pi/2$ to one of the SLMs is equivalent to adding a QWP before the analyzer. Therefore, the set of experimental images in Fig. 3 and Fig. 4 are enough to derive the Stokes parameters in both cases, without requiring a physical QWP. Figures 4(f) and 4(g) represent the right and left circular components of the vector beam in Fig. 3, while Figs. 3(f) and 3(g) represent the left and right circular components of the vector beam in Fig. 4.

Using this technique, we obtained the experimental Stokes parameters images shown in Fig. 5. These images were obtained using standard polarimetric definitions [44]. The case shown in Fig. 5(a), corresponding to the results in Fig. 3, is a radial linear polarized beam. Therefore the ellipticity must be zero, which implies that S_3 is almost zero, whereas S_1 and S_2 varies azimuthally from -1 to $+1$. The case in Fig. 5(b) corresponds to the results in Fig. 4. In this case is the S_2 parameter which remains null over the entire beam, while the S_1 and S_3 parameters show an azimuthal variation. The experimental results agree well with the expected polarization maps.
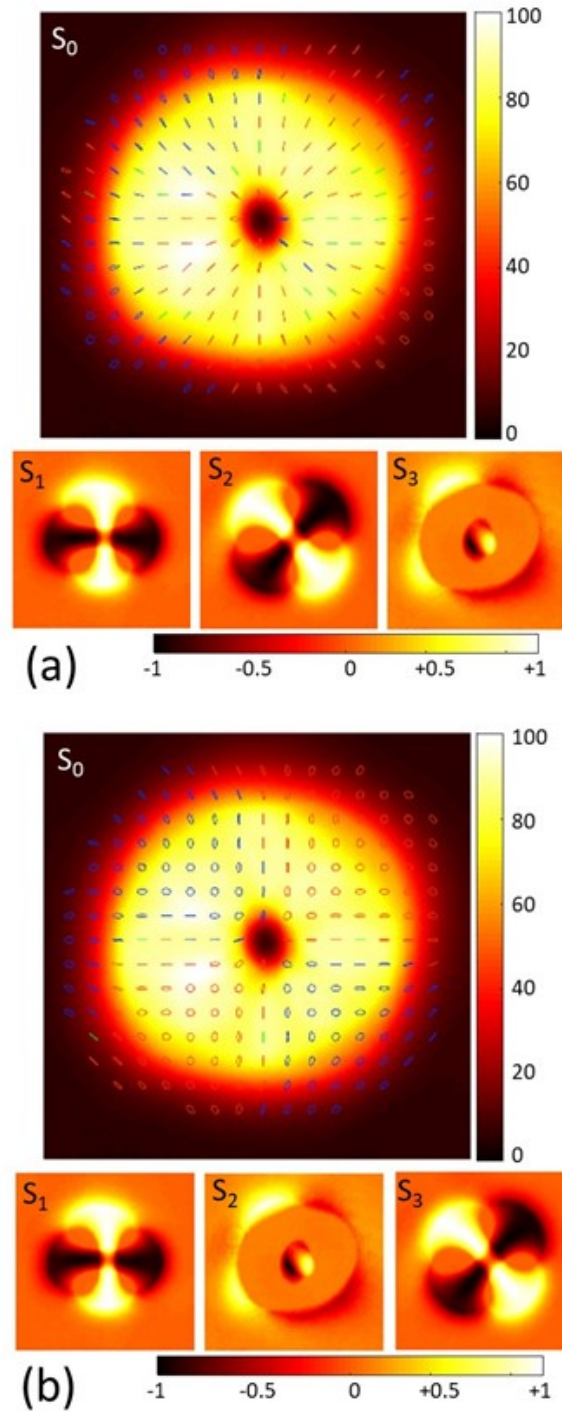
Fig. 5. Images of the experimental Stokes parameters for the vector beams in (a) Figure 3 and (b) Figure 4. S_1, S_2 and S_3 are normalized Stokes parameters.

5.4 Superposition of LG modes to generate HG modes

In this example, we reverse the previous situation and encode $LG_0^{\pm 1}$ modes on the vertical/horizontal polarization components. The results are shown in Fig. 6. Note how the phase holograms in Figs. 6(a) and 6(b) now adopt the shape of a spiral lens, characteristic of combining the spiral phase of LG beams and the quadratic phase of the lens. Notice the opposite sense of rotation, corresponding to the opposite sign of the spiral phase.

14

The output Jones vector can thus be described as:

$$\vec{J}_3(r,\theta) = \frac{1}{\sqrt{2}}\begin{pmatrix} LG_0^1(r,\theta) \\ LG_0^{-1}(r,\theta) \end{pmatrix} = \frac{A_{01}(r)}{\sqrt{2}}\begin{pmatrix} e^{i\theta} \\ e^{-i\theta} \end{pmatrix}, \tag{17}$$

where $A_{01}(r)$ is the radial part of the LG function. This again corresponds to a vector beam, whose polarization pattern is drawn in Fig. 6(c). The state of polarization changes azimuthally due to the phase difference between the horizontal and vertical components. It is always an elliptical state aligned at ±45°, but the ellipticity is changing along the polar coordinate. This again is not a vector beam that belongs to the Poincaré sphere in Fig. 2(c), but it is simply the transmission of the slanted (spiral) polarization state onto a QWP oriented at 45° [43].

When projecting this state onto a linear analyzer oriented at ±45° the following superposition is obtained

$$\vec{J}_{3P} = \frac{1}{2}\begin{pmatrix} 1 & \pm 1 \\ \pm 1 & 1 \end{pmatrix}\vec{J}_3(r,\theta) = \frac{1}{\sqrt{2}}(LG_0^1 \pm LG_0^{-1})\vec{P}_{\pm 45} \propto HG_{10/01}\hat{\mathbf{e}}_{\pm 45,0}, \tag{18}$$

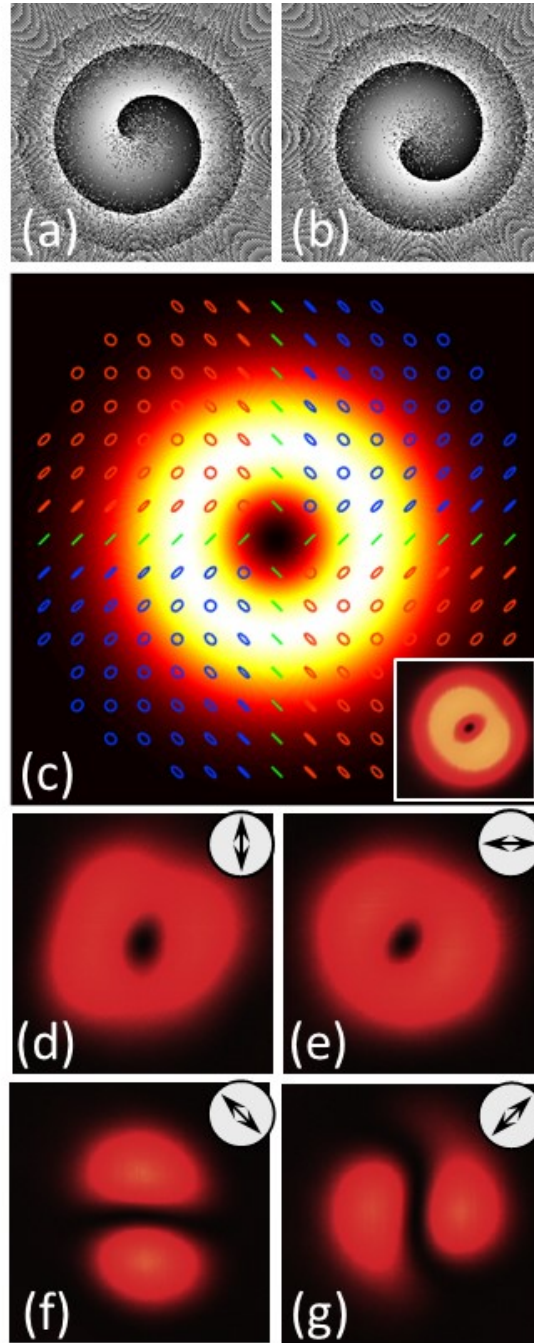which corresponds to the HG modes, according to Eqs. (10).

Fig. 6. (a)-(b) Central part of the phase-only holograms displayed on LCoS1 and LCoS2 to generate LG_0^1 and LG_0^{-1} modes. (c) Expected polarization pattern (the inset shows the CCD capture without analyzer). Ellipses with left- and right-handed polarization are drawn in red and blue respectively. Experimental result with a linear analyzer oriented (d) vertical (LG_0^1), (e) horizontal (LG_0^{-1}), (f) at 45° (HG_{10}) and (g) at −45° (HG_{01}). The analyzer's orientation is indicated on the top of each picture.

Figure 6(d) shows the experimental CCD capture of the generated beam without analyzer, which exhibits the characteristic doughnut shape. However, note in Figs. 6(d) to 6(g) the different projections onto a linear analyzer. When the analyzer is oriented either vertical or horizontal, the LG mode encoded on the corresponding LCoS-SLM is generated. But now, when the analyzer is oriented at ±45° an HG mode is obtained. Namely, at +45°, we get the

16

superposition $LG_0^1 + LG_0^{-1}$, resulting in the HG_{10} mode, while at $-45°$, the superposition is $LG_0^1 - LG_0^{-1}$, resulting in the HG_{01} mode.

5.5 Generation of higher-order modes

In this final subsection we generate higher-order vector beams by combining LG modes, LG_0^ℓ and $LG_0^{-\ell}$ with orthogonal polarization states and higher ℓ values. We used again the linear polarization basis (x, y) that comes from the system in Fig. 1. Therefore, the output vector beam can be written as the following Jones vector:

$$\vec{J}_4(r,\theta) = \frac{1}{\sqrt{2}} \begin{pmatrix} LG_0^\ell(r,\theta) \\ LG_0^{-\ell}(r,\theta) \end{pmatrix} = \frac{A_{0\ell}(r)}{\sqrt{2}} \begin{pmatrix} e^{i\ell\theta} \\ e^{-i\ell\theta} \end{pmatrix}, \tag{19}$$

where $A_{0\ell}(r)$ represents the radial amplitude distribution. Figure 7 shows the experimental results obtained from the superposition of the two modes when the analyzer is oriented at ±45°. The results correspond to the encoding of LG modes with charges $\ell = \pm 2$ (Figs 7(a) and 7(b)) and $\ell = \pm 3$ (Figs 7(c) and 7(d)). They show the characteristic pattern of the so-called petal beams [45], with a total number of four and six lobes respectively.

In Figs. 7(e)-7(h) a more complex superposition is shown. We generate phase-only holograms that encode the modes LG_1^{-3} and LG_0^8 in the vertical and in the horizontal polarization components (Figs. 7(e) and 7(f)). When the analyzer selects one of these two polarizations, the intensity pattern in these two modes arises. However, when the analyzer is oriented at ±45° (Figs. 7(g) and 7(h)), the petal interference pattern is observed only in the external ring.
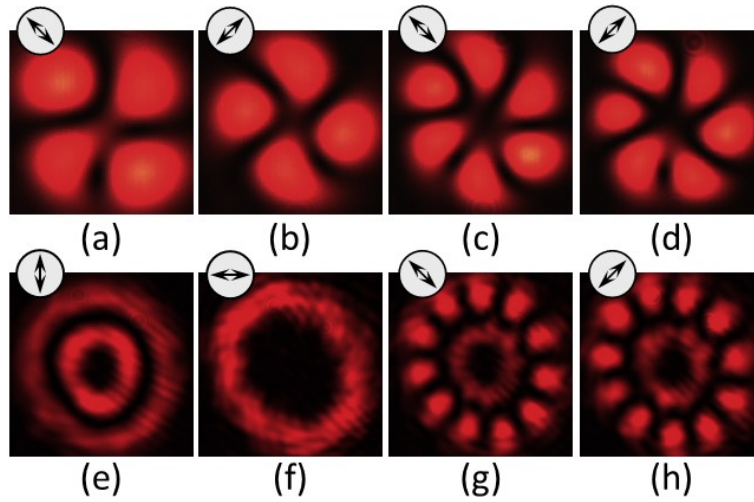

Fig. 7. Experimental CCD captures of the following cases: (a) $LG_0^2 + LG_0^{-2}$, (b) $LG_0^2 - LG_0^{-2}$, (c) $LG_0^3 + LG_0^{-3}$, (d) $LG_0^3 - LG_0^{-3}$, (e) LG_1^{-3}, (f) LG_0^8, (g) $LG_1^{-3} + LG_0^8$, (h) $LG_1^{-3} - LG_0^8$. The orientation of the analyzer is indicated on the top of each picture.

6. PHASE EVALUATION WITH PROGRAMMED PHASE-SHIFTING

One of the great advantages of using SLMs to generate these modes is the ability to program arbitrary phase holograms. The previous results have demonstrated the accurate generation of the intensity pattern characteristic of different types of modes. However, in order to completely

verify that we are indeed generating the correct vector beam, the phase distribution of the superposition beams should be measured as well. This requires interferometric techniques. In this section we show that our SLM-based optical setup can be employed to perform this phase evaluation through phase-shifting interferometry (PSI) and without requiring any other additional elements.

Phase-shifting interferometry (PSI) [46] uses multiple interferograms with different relative phase shift between the reference and the test beams. We use the four-step algorithm with phase shifts 0, $\pi/2$, π, and $3\pi/2$. A similar approach was used in [35] to evaluate the phase of scalar beams generated with a single SLM. Here we extend it to the case of the generated VBs. The interferograms are obtained simply by placing a final analyzer oriented at ±45° before the CCD detector. Then, the required relative phase shift is introduced in one of the modulators, with steps of $\pi/2$ phase shift. Four images are captured, $I(x, y; \delta)$, one for each value of the phase shift δ, and the spatial phase distribution $\Delta(x, y)$ is calculated as

$$\Delta(x, y) = \arctan\left[\frac{I\left(x, y; \frac{3\pi}{2}\right) - I\left(x, y; \frac{\pi}{2}\right)}{I(x, y; 0) - I(x, y; \pi)}\right]. \tag{20}$$

Figures 8(a) and 8(b) show the generation of two LG_0^ℓ modes, having $\ell = \pm 5$, respectively. Their superposition is presented in Fig. 8(c) when the analyzer is oriented at 45°, and results in a petal beam with ten lobes. The result of the phase-shift algorithm is shown in Fig. 8(d). We can observe that the experimental superposition $LG_0^5 + LG_0^{-5}$ shows spiral phase pattern with $2\ell = 10$ jumps from 0 to 2π, thus verifying the correct generation of the beam.

A more complex situation is shown in the second row of Fig. 8. In this case, the vertical and horizontal polarization components encode modes LG_0^7 and LG_0^{-2} respectively. The difference in the magnitude of ℓ is noticeable in the different diameter of the two rings. When the analyzer is oriented at 45° to generate their superposition, the intensity pattern shows a null point at the center, but additional nine dark points around it (Fig 8(g)). The measured phase associated to this intensity pattern is displayed in Fig. 8(h) and exhibits nine phase jumps from 0 to 2π along the polar coordinate.
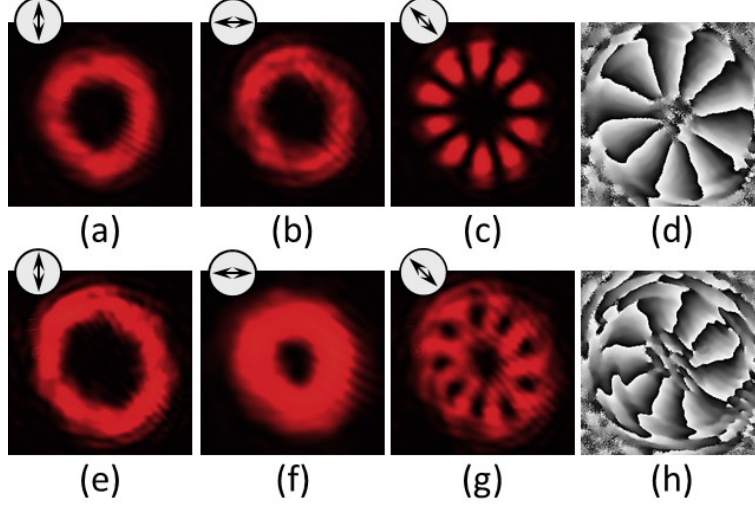
Fig. 8. Experimental CCD captures of: (a) LG_0^5, (b) LG_0^{-5}, (c) $LG_0^5 + LG_0^{-5}$. (d) Phase of (c) measured using PSI. Experimental CCD captures of: (e) LG_0^7, (f) LG_0^{-2}, (g) $LG_0^7 + LG_0^{-2}$. (h) Phase of (g) measured using PSI.

7. CONCLUSIONS

In summary, we have presented an optical setup using a Z-configuration which is based on two LCoS panels working in phase-only modulation useful to generate different vector modes that result from the superposition of HG and LG modes encoded on orthogonal linear polarizations. A remarkable advantage of this optical arrangement is its high light-efficiency, since no beam splitter is employed. In addition, since the SLMs used in this work do not show flicker, they can be operated in the zero diffraction order (there is no need of a phase carrier). Consequently, the complete space-bandwidth product of the device is employed and we can work on-axis. The optical system energy budget is reduced mainly by the reflectivity ($R\sim78\%$) and the zero-order diffraction efficiency ($\eta\sim96\%$) of the LCoS devices. Since two LCoS-SLMs are employed, the total system maximum conversion efficiency is about 56% (additional losses at the lenses and HWP in the system should also be accounted).

We use the LCoS-SLMs to encode spatial patterns that modify the phase but also the magnitude of the vertical and horizontal polarization components. For that purpose, a recently developed technique to encode complex functions in phase-only functions is applied [35], which also reconstructs the desired field on axis. The encoding technique introduces additional losses that depend on the magnitude information that is encoded. Magnitude encoding is accomplished by diffracting light out of axis by means of a diverging axicon whose characteristic Fourier transform ring must be filtered. Nevertheless, the encoding technique generates on-axis hologram reconstruction, thus avoiding any additional phase carrier function. The experimental realization of different vector beams has been demonstrated.

Finally, another interesting result of our proposal relies on the fact that with the same optical setup, the calculation of the phase distribution of the resulting vector beams can be easily retrieved. We use a four-step phase-shifting algorithm to evaluate the phase of the generated beams even for higher orders. As a result, we have developed an efficient facility to generate different types of vector beams, useful for developing complex light beams that could be exploited in any of the many applications of vector beams that are nowadays developed.

REFERENCES

[1]. R. Dorn, S. Quabis, and G. Leuchs, "Sharper focus for a radially polarized light beam" Phys. Rev. Lett. **91**, 233901 (2003).

[2]. B. J. Roxworthy and K. C. Toussaint, Jr., "Optical trapping with π-phase cylindrical vector beams," New. J. Phys. **12**, 073012 (2010).

[3]. Y. Jin, O. J. Allegre, W. Perrie, K. Abrams, J. Ouyang, E. Fearon, S. P. Edwardson, and G. Dearden, "Dynamic modulation of spatially structured polarization fields for real-time control of ultrafast laser-material," Opt. Express **21**, 25333–25343 (2013).

[4]. P. Török and P. R. T. Munro, "The use of Gauss-Laguerre vector beams in STED microscopy," Opt. Express **12**, 3605–3617 (2004).

[5]. Q. Zhan, "Cylindrical vector beams: from mathematical concepts to applications," Adv. In Opt. Photon. **1**, 1-57 (2009).

[6]. A. Forbes, *Laser Beam Propagation. Generation and Propagation of Customized Light,* (CRC, Pretoria, 2014).

[7]. C. Rosales-Guzmán, B. Ndagano, and Andrew Forbes, "A review of complex vector light fields and their applications," J. Opt. **12**, 123001 (2018).

[8]. Y. Mushiake, K. Matsumura, and N. Y. Nakajima, "Generation of radially polarized optical beam mode by laser oscillation," Proc. IEEE 60, 1107 (1972).

[9]. S. C. Tidwell, D. H. Ford, and W. D. Kimura, "Generating radially polarized beams interferometrically", Appl. Opt. **29** 2234–9 (1990).

[10]. Z. Bomzon, G. Biener, V. Kleiner, and E. Hasman, "Radially and azimuthally polarized beams generated by space-variant dielectric subwavelength gratings" Opt. Lett. **27** 285–287 (2002).

[11]. M. Stalder and M. Schadt, "Linearly polarized light with axial symmetry generated by liquid-crystal polarization converters," Opt. Lett. **21**, 1948-1950 (1996).

[12]. L. Marrucci, C. Manzo, and D. Paparo, "Optical spin-to-orbital angular momentum conversion in inhomogeneous anisotropic media," Phys. Rev. Lett. **96**, 163905 (2006).

[13]. F. Cardano, E. Karimi, S. Slussarenko, L. Marrucci, C. de Lisio, and E. Santamato, "Polarization pattern of vector vortex beams generated by *q*-plates with different topological charges", Appl. Opt. **51** (10), C1-C6 (2012).

[14]. M. Rafayelyan and E. Brasselet, "Laguerre–Gaussian modal *q*-plates", Opt. Lett. **42**, 1966-1969 (2017).

[15]. C. Maurer, A. Jesacher, S. Fürhapter, S. Bernet, and M. Ritsch-Marte, "Tailoring of arbitrary optical vector beams", New J. Phys. **9**, 78 (2007).

[16]. I. Moreno, M. M. Sánchez-López, K. Badham, J. A. Davis, D. M. Cottrell, "Generation of integer and fractional vector beams with *q*-plates encoded onto a spatial light modulator," Opt. Lett. **41** (6), 1305-1308 (2016).

[17].E. J. Galvez, S. Khadka, W. H. Schubert, and S. Nomoto, "Poincaré-beam patterns produced by nonseparable superpositions of Laguerre–Gauss and polarization modes of light," Appl. Opt. **51**, 2925-2934 (2012).

[18].E. Otte, K. Tekce and C. Denz, "Spatial multiplexing for tailored fully-structured light," J. Opt. **20**, 105606 (7pp) (2018).

[19].I. Moreno, J. A. Davis, K. Badham, M. M. Sánchez-López, J. E. Holland, and D. M. Cottrell, "Vector beam polarization state spectrum analyzer," Scientific Rep. **7**, 2216 (2017).

[20].C. Rosales-Guzmán, N. Bhebhe, and A. Forbes, "Simultaneous generation of multiple vector beams on a single SLM," Opt. Express **25** (21), 25697-25706 (2017).

[21].K. J. Mitchell, N. Radwell, S. Franke-Arnold, M. J. Padgett, and D. B. Phillips, "Polarisation structuring of broadband light", Opt. Express **25** (21), 25079-25089 (2017).

[22].S. Ngcobo, I. Litvin, L. Burger, and A. Forbes, "A digital laser for on-demand laser modes", Nat. Communications **4**, 2289 (2013).

[23].D. Naidoo, F. S. Roux, A. Dudley, I. Litvin, B. Piccirillo, L. Marrucci, and A. Forbes, "Controlled generation of higher-order Poincaré sphere beams from a laser", Nat. Photonics **10**, 327-333 (2016).

[24].M.-Q. Cai, Z.-X. Wang, J. Liang, Y.-K. Wang, X.-Z. Gao, Y. Li, C. Tu, and H.-T. Wang, "High-efficiency and flexible generation of vector vortex optical fields by a reflective phase-only spatial light modulator", Appl. Opt. **56** (22), 6175-6180 (2017).

[25].S. Liu, S. Qi, Y. Zhang, P. Li, D. Wu, L. Han, and J. Zhao, "Highly efficient generation of arbitrary vector beams with tunable polarization, phase, and amplitude", Photonics Res. **6** (4), 228-233 (2018).

[26].J. A. Davis, D. M. Cottrell, J. Campos, M. J. Yzuel, and I. Moreno, "Encoding amplitude information onto phase-only filters," Appl. Opt. **38**, 5004-5013 (1999).

[27].T. W. Clark, R. F. Offer, S. Franke-Arnold, A. S. Arnold, and N. Radwell, "Comparison of beam generation techniques using a phase only spatial light modulator," Opt. Express **24**, 6249 (2016).

[28].J. B. Bentley, J. A. Davis, M. A. Bandres, and J. C. Gutiérrez-Vega, "Generation of helical Ince-Gaussian beams with a liquid crystal display," Opt. Lett. **31** (5), 649-651 (2006).

[29].L. Zhu and J. Wang, "Arbitrary manipulation of spatial amplitude and phase using phase-only spatial light modulators" Scientific Rep. **4**, 7441 (2014).

[30].D. Aguirre-Olivas, G. Mellado-Villaseñor, D. Sanchez-de-la-llave, and V. Arrizón, "Efficient generation of Hermite-Gauss and Ince-Gauss beams through kinoform phase elements," Appl. Opt. **54**, 8444-8452 (2015).

[31].A. Lizana, I. Moreno, A. Márquez, C. Iemmi, E. Fernández, J. Campos, M. J. Yzuel, "Time fluctuations of the phase modulation in a liquid crystal on silicon display: characterization and effects in diffractive optics," Opt. Express **16**, 16711-16722 (2008).

[32].B. Khajavi and E. J. Galvez, "High-order disclinations in space-variant polarization," J. Opt. **18** (8), 084003 (2016).

[33].A. Cofré, A. Vargas, F. A. Torres-Ruiz, J. Campos, A. Lizana, M. M. Sánchez-López, and I. Moreno, "Quantitative performance of a polarization diffraction grating polarimeter encoded onto two liquid-crystal-on-silicon displays", Opt. Laser Technol. **96**, 219–226 (2017).

[34].A. Cofré, A. Vargas, F. A. Torres-Ruiz, J. Campos, A. Lizana, M. M. Sánchez-López, and I. Moreno, "Dual polarization split lenses", Opt. Express **25** (20), 23773-23783 (2017).

[35]. J. L. Martínez-Fuentes and I. Moreno, "Random technique to encode complex valued holograms with on axis reconstruction onto phase-only displays", Opt. Express **26** (5), 5875-5893 (2018).

[36]. N. Suchkov, E. J. Fernandez, J. L. Martinez-Fuentes, I. Moreno, and P. Artal "Simultaneous aberration and aperture control using a single spatial light modulator," Opt. Express (2019), in press.

[37]. E. J. Galvez, "Vector beams in free space", Chap. 3 in *The Angular Momentum of Light*, D. L. Andrews, M. Bebiker Edts., Cambridge University Press (2013).

[38]. M. J. Padgett and J. Courtial, "Poincaré-sphere equivalent for light beams containing orbital angular momentum," Opt. Lett. **24** (7), 430-432 (1999).

[39]. G. Milione, H. I. Sztul, D. A. Nolan, and R. R. Alfano, "Higher-order Poincaré sphere, Stokes parameters, and the angular momentum of light," Phys. Rev. Lett. **107**, 053601 (2011).

[40]. L. Marrucci, "Liquid crystal "q-plates": classical and quantum photonic applications," Proc. SPIE 8475, 84750P (2012).

[41]. J. A. Davis, N. Hashimoto, M. Kurihara, E. Hurtado, M. Pierce, M. M. Sánchez-López, K. Badham, and I. Moreno, "Analysis of a segmented *q*-plate tunable retarder for the generation of first-order vector beams," Appl. Opt. **54** (31), 9583-9580 (2015).

[42]. H. Sroor, I. Litvin, D. Naidoo, A. Forbes, "Amplification of higher-order Poincaré sphere beams through Nd:YLF and Nd:YAG crystals", Appl. Phys. B **125**, 49 (2019).

[43]. I. Moreno, J. Albero, J. A. Davis, D. M. Cottrell, J. B. Cushing, "Polarization manipulation of radially polarized beams," Opt. Eng. **51** (12), 128003 (2012).

[44] D. Goldstein, Polarized Light, 2nd Edt. (Marcel Dekker, 2003).

[45]. I. A. Litvin, L. Burger, and A. Forbes, "Angular self-reconstruction of petal-like beams," Opt. Lett. **38** (17), 3363-3365 (2013).

[46]. H. Schreiber and J. H. Bruning, "Phase shifting interferometry", Ch. 7 in D. Malacara (Edt.) *Optical Shop Testing*, 3rd edtn. (John Wiley & Sons, Hoboken, 2007).